The Astrophysical Journal Letters, 891:L25 (8pp), 2020 March 1 https://doi.org/10.3847/2041-8213/ab7750

Plasma Emission Induced by Electron Cyclotron Maser Instability in Solar Plasmas with a Large Ratio of Plasma Frequency to Gyrofrequency

Sulan Ni[1], Yao Chen[1], Chuanyang Li[1], Zilong Zhang[1], Hao Ning[1], Xiangliang Kong[1], Bing Wang[1], and M. Hosseinpour[2]
[1] Institute of Space Sciences, Institute of Frontier and Interdisciplinary Science, Shandong University, Shandong, People's Republic of China; yaochen@sdu.edu.cn
[2] Faculty of Physics, University of Tabriz, Tabriz, Iran
Received 2020 January 2; revised 2020 February 14; accepted 2020 February 17; published 2020 March 4

Abstract

In plasmas with a large ratio of plasma frequency to gyrofrequency (ω_{pe}/Ω_{ce}), energetic electrons characterized by $\partial f/\partial v_\perp > 0$ can excite electron cyclotron maser instability (ECMI), generating waves of upper hybrid (UH), Z, and W modes. It has been presumed that these ECMI waves can somehow convert to escaping X–O modes as fundamental (F) or harmonic (H) plasma emission. Here we perform a fully kinetic, electromagnetic particle-in-cell simulation to investigate the proposed radiation process. ECMI is driven by energetic electrons with a Dory–Guest–Harris distribution representative of a double-sided loss cone, and ω_{pe}/Ω_{ce} is set to be 10. We find that the electrostatic UH mode is the fastest-growing mode. Around the time when its energy starts to decline, the W mode grows to be dominant. During this stage, we observe significant F and H plasma emission. The F emission is in the O mode with a bandwidth around 0.1–0.2 Ω_{ce}, and the H emission is contributed by both X and O modes with a narrower bandwidth. We suggest that the O–F emission is caused by coalescence of almost counterpropagating Z and W modes, while the H emission arises from coalescence of an almost counterpropagating UH mode at relatively large wave number. Thus the plasma emission investigated here is induced by a combination of wave growth due to ECMI and further nonlinear wave-coupling processes. The result is relevant to understanding solar radio bursts as well as other astronomical radio sources that are excited by energetic electrons trapped within certain magnetic structures.

Unified Astronomy Thesaurus concepts: Solar corona (1483); Solar activity (1475); Radio bursts (1339); Solar coronal radio emission (1993); Plasma astrophysics (1261)

Supporting material: animations

1. Introduction

We define solar radio bursts as enhanced radiation escaping from the solar atmosphere, observed in a wide range of wavelengths from centimetric to kilometric (Wild et al. 1963; McLean & Labrum 1985; Pick & Vilmer 2008). They are generated by energetic electrons released during solar activities, such as flares, coronal mass ejections, and small-scale EUV brightenings associated with type-I bursts (see, e.g., Li et al. 2017). Spectral and imaging observations of these bursts can be used to infer properties of coronal plasmas and magnetic fields, energetic electrons, and dynamic processes of solar activities, given enough knowledge of the underlying emission mechanisms.

Both incoherent emission, for instance, the gyro-synchrotron radiation of electrons circling around a coronal magnetic field (see e.g., Ramaty 1969; Dulk & Marsh 1982), and coherent emission (Ginzburg & Zhelezniakov 1958; Wu & Lee 1979; Melrose & Dulk 1982) have been proposed to explain solar radio bursts. For coherent emission, the proposed mechanisms can be grouped into two classes. The first class is the plasma emission mechanism induced by kinetic bump-in-tail instability driven by beams of energetic electrons. The theory was first outlined by Ginzburg & Zhelezniakov (1958) and subsequently further modified (see the latest review by Melrose 2017). According to these studies, the plasma emission is an indirect multi-stage process including generation of enhanced Langmuir waves, their scattering over ion acoustic waves or density structures to generate the fundamental emission and/or backward-propagating Langmuir waves, and nonlinear wave–wave coalescence to yield the harmonic emission. Recent numerical studies support the occurrence of this multi-stage process within a single-beam system using multi-dimensional, fully kinetic and electromagnetic particle-in-cell (PIC) simulations (e.g., Thurgood & Tsiklauri 2015; Henri et al. 2019).

The other type of coherent emission mechanism is electron cyclotron maser emission (ECME), which can linearly amplify escaping electromagnetic radiation through resonant wave–particle interaction, and thus represents a direct emission process (Wu & Lee 1979). ECME is induced by population inversion of energetic electrons in velocity space along the perpendicular direction, i.e., with $\partial f/\partial v_\perp > 0$. Note that the possibility of direct amplification of radiation at frequencies close to Ω_{ce} and its harmonics through resonant interaction between waves and energetic electrons was originally suggested by Twiss (1958), Gaponov (1959), and Schneider (1959), and reviewed by Wu (1985), Treumann (2006), and Melrose (2017). Wu & Lee (1979) were the first to recognize the importance of relativistic correction in the resonance condition, even for weakly relativistic electrons, and achieved major progress in the development of ECME theory.

It is well known that ECME can be excited by energetic electrons with a loss-cone or ring-type velocity distribution in plasmas with $\omega_{pe}/\Omega_{ce} < 1$. Therefore, most existing studies on ECME were for plasmas within this parameter regime. Solar coronal plasmas, however, mostly lie in the regime of $\omega_{pe}/\Omega_{ce} > 1$, especially for plasmas in the outer corona. This puts strong limits on the applicability of ECME to the various types of solar radio bursts that are frequently observed within metric wavelengths at relatively high altitude above the disk, such as type-IV radio bursts (see, e.g., Vasanth et al.

2016, 2019; Liu et al. 2018 for latest studies), type-II (Feng et al. 2013; Chen et al. 2014; Kong et al. 2015; Lv et al. 2017 for latest studies), type-I (e.g., Li et al. 2017), and type-N (e.g., Kong et al. 2016).

Within the parameter regime of $\omega_{\rm pe}/\Omega_{ce} > 1$, growth rates of X and O modes become smaller than those of the non-escaping Z and W modes at lower frequencies (e.g., Winglee 1985; Wu 1985; Yi et al. 2013). Note that, due to thermal effects, the Z-mode frequency can exceed its cold plasma cutoff at the upper hybrid (UH) frequency. This affects the wave growth (see, e.g., Li et al. 2019) and a kinetic treatment is necessary. Winglee & Dulk (1986a) proposed that electrostatic UH waves, generated by electron cyclotron maser instability (ECMI) at frequencies close to $\omega_{\rm UH} \sim \omega_{\rm pe}$, can convert through wave–wave coalescence into transverse escaping X–O mode radiation. This can be considered as a radiation mechanism combining both ECMI and nonlinear wave–wave interaction of the classical plasma emission process, and has been suggested to explain type-IV and type-V solar radio bursts (Winglee & Dulk 1986a, 1986b; Vasanth et al. 2019).

Many subsequent studies have investigated the excitation of UH or Z mode driven by distributions such as loss-cone, ring-beam, or Dory–Guest–Harris (DGH; Dory et al. 1965) (e.g., Sharma & Vlahos 1984; Stepanov et al. 1999; Lee et al. 2009, 2011; Yi et al. 2013). In particular, the intriguing zebra patterns observed during type-IVs have been considered as a direct result of variations of the maximum growth rate and corresponding frequency of the UH mode with $\omega_{\rm pe}/\Omega_{\rm ce}$ (Winglee & Dulk 1986a; Yasnov & Karlický 2004; Zlotnik 2013; Benáček et al. 2017; Li et al. 2019). These studies reveal that the maximum growth rates of electrostatic UH modes have peaks at frequencies around $s\Omega_{\rm ce}$, where s is a positive integer, in accordance with the observation of the zebra stripes. However, most studies simply assumed that the electrostatic mode excited via ECMI could be further converted to escaping radiation through some nonlinear coalescence process and did not investigate any details of such a process. Only a few studies have investigated the coalescence process using analytic methods (Melrose 1991; Stepanov et al. 1999).

It is apparent that a fully kinetic electromagnetic PIC simulation is necessary to understand the complete ECMI–plasma emission process. Most earlier PIC simulations of radiation excited by ECMI were carried out in the parameter regime of $\omega_{\rm pe}/\Omega_{ce} < 1$ (e.g., Wagner et al. 1984; Pritchett 1986; Lee et al. 2009), i.e., for the direct ECME process, while existing PIC simulations for $\omega_{\rm pe}/\Omega_{ce} > 1$ have not taken wave coupling into account. For example, Lee et al. (2018) investigated the excitation of a magnetospheric Bernstein mode using a one-dimensional relativistic electromagnetic PIC simulation, and Benáček & Karlický (2018) investigated the change of growth rate of UH waves with varying $\omega_{\rm pe}/\Omega_{\rm ce}$. Both studies described the excitation of electrostatic modes by some prescribed DGH distribution, without considering the generation of escaping electromagnetic radiation. Thus, the complete emission process from excitation of electrostatic ECMI waves to escaping plasma radiation with $\omega_{\rm pe}/\Omega_{ce} \gg 1$ has never been simulated, to the best of our knowledge. It is the aim of the present study to demonstrate that this process does occur in a plasma system with fully kinetic multi-dimensional and electromagnetic PIC simulations.

2. The Vector-PIC Code and Parameter Setup of Simulations

The numerical simulation reported here is performed using the Los Alamos National Labs Vector-PIC (VPIC) code, which was run on the Tianhe-2 and Tianhe-3 supercomputer systems. As a general purpose PIC code for modeling kinetic plasmas, VPIC employs a second-order, explicit, leapfrog algorithm to update charged particle positions and velocities in order to solve the relativistic kinetic equation for each species, along with a full Maxwell description for electric and magnetic fields evolved via a second-order finite-difference time-domain solver (Bowers et al. 2008a, 2008b, 2009). VPIC includes a flexible input deck format so that it can treat a wide variety of problems (Li et al. 2015; Guo et al. 2016).

The simulations are run in two spatial dimensions (2D) with three vector components (3V). The background magnetic field is set to be $\boldsymbol{B}_0$ ($=B_0\hat{e}_z$), and the wave vector ($\boldsymbol{k}$) within the xOz plane, thus E_y represents the pure transverse component of the wave electric field. Periodic boundary conditions are used. The plasmas consist of background electrons and protons with a Maxwellian distribution, and energetic electrons with the DGH distribution ($j = 1$), as follows:

$$f_0 = \frac{1}{(2\pi)^{3/2}v_0^3}\exp\left(-\frac{u^2}{2v_0^2}\right) \quad (1)$$

$$f_e = \frac{u_\perp^{2j}}{2^j(2\pi)^{3/2}v_{\rm e}^{3+2j}j!}\exp\left(-\frac{u_\parallel^2 + u_\perp^2}{2v_{\rm e}^2}\right) \quad (2)$$

where u_x, u_y, u_z are momentum per mass of particles, $v_0 = 0.018c$ (~2 MK) and $v_{\rm e} = 0.3c$, and c is the speed of light. Protons are initialized with the same thermal speed v_0. All particles are distributed uniformly in space.

The initial distribution of electrons is plotted in Figure 1(a). It can be seen that the DGH distribution represents an enhancement of the population of energetic electrons around large pitch angles. This distribution, widely used in previous investigations, is regarded as a kind of double-sided loss cone, which may develop when energetic electrons are injected and trapped within magnetic structures.

As stated, we are mainly interested in radio emissions released from plasmas characterized by $\omega_{\rm pe}/\Omega_{\rm ce} \gg 1$, therefore this ratio is set to be 10. The effect of $\omega_{\rm pe}/\Omega_{\rm ce}$ on wave excitation and radiation processes will be investigated in future.

The domain of the simulation is set to be $L_x = L_z = 1024\ \Delta$, where $\Delta = 3.25\ \lambda_D$ is the grid spacing, and λ_D is the Debye length of background electrons. The unit of length is the electron inertial length ($d_{\rm e} = c/\omega_{\rm pe}$) and the unit of time is the plasma response time ($\omega_{\rm pe}^{-1}$). The simulation lasts for 3500 $\omega_{\rm pe}^{-1}$. The wave number range that can be resolved is [−536, 536] Ω_{ce}/c, and that of resolvable frequency is [0, 32] $\Omega_{\rm ce}$. Charge neutrality is maintained by employing the same amount of protons. A realistic proton-to-electron mass ratio of 1836 is used, and the number density ratio of DGH to total electrons is assumed to be 0.1. We include 2000 macroparticles for each species in each cell.

3. Numerical Results

In Figure 1, we present the velocity distribution in $v_\perp$–$v_\parallel$ phase space (panels (a)–(d)) at four representative moments with an accompanying movie. The distribution starts to evolve

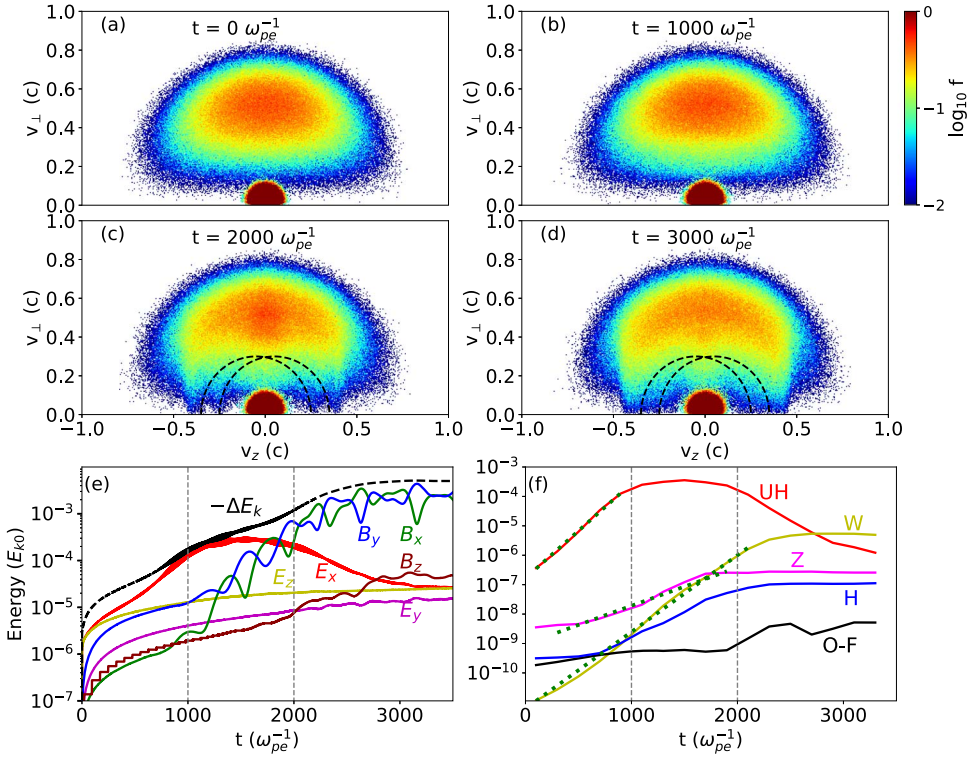

Figure 1. (a)–(d) Snapshots of the initial background plus Dory–Guest–Harris (DGH) velocity distribution function, at $\omega_{pe}t = 0$, 1000, 2000, and 3000; (e) temporal profiles of energies of various field components (E_x, E_y, E_z, B_x, B_y, and B_z) normalized to the initial kinetic energy of DGH electrons (E_{k0}); (f) temporal profiles of electric field energies of various wave modes normalized to E_{k0}, with "UH" for upper hybrid mode, "W" for whistler mode, "Z" for Z mode, "O–F" for O mode around the fundamental plasma frequency, and "H" for harmonic plasma emission. The two dashed arcs plotted in panels (c) and (d) are diffusion curves of the W mode, the two dashed lines in panels (e) and (f) denote intervals corresponding to stages I, II, and III, and the three dotted lines in panel (f) represent exponential fittings to energy profiles. An animation of this figure (panels (a)–(d)) is available. The video begins at $\omega_{pe}t = 0$ and ends at $\omega_{pe}t = 3000$. The realtime duration of the video is 6 s.

(An animation of this figure is available.)

significantly from 1500 to 2000 ω_{pe}^{-1}, with electrons diffusing from larger to smaller $v_\perp$, leading to gradual filling up of the loss cones. A substantial portion has been filled after $t = 3000\ \omega_{pe}^{-1}$.

The temporal profiles of energy of various field components are plotted in Figure 1(e), normalized by the initial kinetic energy of DGH electrons (E_{k0}). The evolution of relative decline of E_{k0} ($-\Delta E_k$) is over-plotted. In between 0 and 1000 ω_{pe}^{-1}, E_x increases rapidly by ~2 orders of magnitude above the corresponding noise level and becomes the dominant component in energy. Between 1000 and 2000 ω_{pe}^{-1}, the energy of E_x remains the strongest component. In the meantime, the two perpendicular components of magnetic field (B_x and B_y) start to rise rapidly. Up to ~2500 ω_{pe}^{-1}, the energy of E_x becomes weaker by one order of magnitude than its peak value, and B_x and B_y become the dominant components. The energies of B_x and B_y reach a very high level ($\sim 10^{-3}\ E_{k0}$) around t ~2500 ω_{pe}^{-1} and maintain this level until their saturation. According to the energy profiles, we split the system evolution into three stages, stage I ($0 \sim 1000\ \omega_{pe}^{-1}$), II ($1000 \sim 2000\ \omega_{pe}^{-1}$), and III ($2000 \sim 3500\ \omega_{pe}^{-1}$). From the following wave dispersion analysis, it can be seen that stage I is characterized by rapid growth of the UH mode represented by E_x, stage II by the plateau of its intensity together with rapid growth of the W mode (mainly carried by B_x and B_y), and stage III by gradual saturation of these modes.

The profile of $-\Delta E_k$ closely follows the increase of E_x in stage I and the increase of B_x and B_y in stage II. This means that the growth of waves is at the expense of E_{k0}. The magnitude of $-\Delta E_k$ remains at an almost constant level around $2 \times 10^{-3}\ E_{k0}$ in stage III since the energy-dominant wave modes approach their saturation levels.

The electron scattering observed from the velocity distribution is mainly due to the W mode, according to the wave dispersion analysis to be presented. Its frequency is below, yet still considerably close to, Ω_{ce} and thus can interact strongly with electrons. This is supported by the observation that significant scattering occurs along with the rapid growth of B_x and B_y. To further show this, we over-plot two diffusion curves of the W mode in panels (c) and (d) of Figure 1. These two diffusion curves correspond to forward- and backward-propagating W modes, respectively, with typical phase speed of $\sim 0.05c$ according to the simulation.

In Figure 2, we present the wave-energy distribution in the wave vector space ($k_\parallel$, $k_\perp$) for the three stages using the components of the electric field. Panel (d) is a zoom-in version of panel (c). For each stage, the maximum wave intensities at the corresponding wave vector are exhibited in color. One substantial feature of this figure is that all panels manifest symmetric patterns of wave growth, due to the symmetry of the DGH distribution in velocity space.

In stage I, the strongest waves are those in dark elliptical regions centered along the vertical direction at relatively large wave numbers ($25\ \Omega_{ce}/c \leqslant |k| \leqslant 80\ \Omega_{ce}/c$); see the panel for E_x. Correspondingly, in the E_z map around a similar range of $|k|$, there also appears significant wave growth. Note that, in

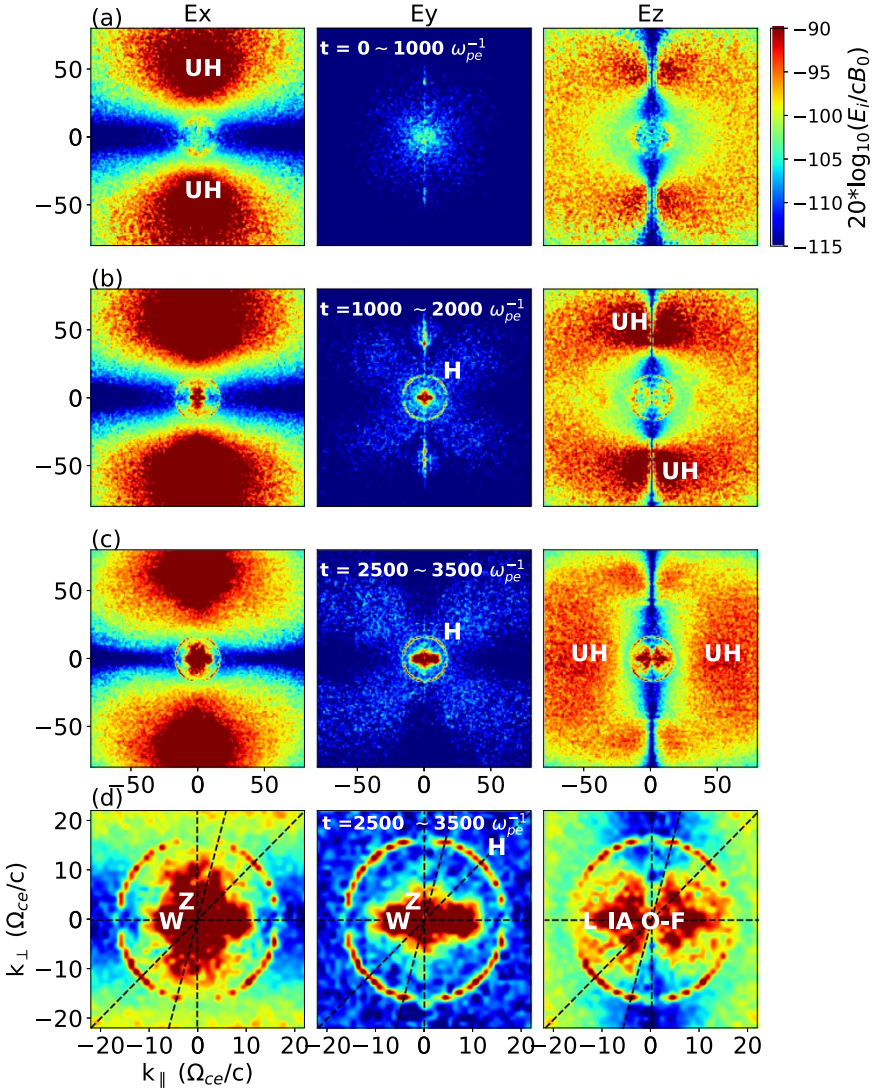

Figure 2. Maximum intensity of (E_x, E_y, E_z) in the ω domain as a function of $k_\parallel$ and $k_\perp$ over intervals of (a) $0 < \omega_{pe}t < 1000$, (b) $1000 < \omega_{pe}t < 2000$, and (c) $2500 < \omega_{pe}t < 3500$, as shown by the colormap of 20 log_{10} [(E_x, E_y, E_z)/(cB_0)]; panel (d) is a zoom-in version of panel (c). All panels use the same colorbar as shown next to panel (a). In addition to the terms defined in Figure 1, "L" stands for Langmuir mode, and "IA" is for ion acoustic mode. The three dashed lines plotted in panel (d) are the directions of dispersion analysis (see Figures 3 and 4).

contrast to the energy map of E_x, the E_z map presents negligible wave growth along the perpendicular direction. This growth of E_x and E_z at relatively large $|k|$ is associated with the UH mode according to the following analysis. At smaller wave numbers ($|k| \leqslant 20\ \Omega_{ce}/c$) there appear other groups of waves identified as X–Z and O–W modes, according to magneto-ionic theory. These modes can be better identified from the zoom-in version of wave distribution (panel (d)). We see that for stages II and III there is a circular region of significant wave growth with $|k| \sim 16.5\ \Omega_{ce}/c$, corresponding to the harmonic electromagnetic emission at $\sim 19.0\ \Omega_{ce}$. Within the circular region are the W mode mainly along the parallel (and anti-parallel) direction and Z mode along the perpendicular and oblique direction. It is difficult to identify the F emission of the X and O modes from this figure since their intensities are in general weaker than those discussed above.

During stage I the UH mode is the fastest-growing, while during stage II the W mode becomes fastest and the UH mode ceases its rapid growth. The circular H emission appears in both stages II and III, and its intensity remains almost unchanged. In Figure 3, we resort to spectral analysis of the wave dispersion ($\omega - k$) to further explore the characteristics of these modes.

To exhibit the UH mode at large wave number, we show the analysis for $|k| \leqslant 60\ \Omega_{ce}/c$ at different propagation angles in Figure 3 and the accompanying movie. Again the symmetric pattern of wave growth is obvious.

Another obvious feature of this figure is significant wave enhancement around ω_{pe}. In thermal plasmas, these waves represent the Langmuir (L) mode and its obliquely propagating counterpart. Due to the presence of DGH electrons, the spectrum around ω_{pe} is broken into two parts. One part is still L and Z modes along different directions with relatively small wave number ($|k| < 15\ \Omega_{ce}/c$); the other part starts from $|k| \sim 25\ \Omega_{ce}/c$ and extends to $\sim 80\ \Omega_{ce}/c$. The L–Z modes extend to higher frequency with increasing $|k|$ due to thermal effects. The L mode with $\theta_{kB} = 0°$ is an electrostatic one while the obliquely propagating Z mode at $\omega \leqslant \omega_{pe}$ contains significant magnetic components, and the Z mode above ω_{pe} is mostly electrostatic due to the effect of upper-hybrid

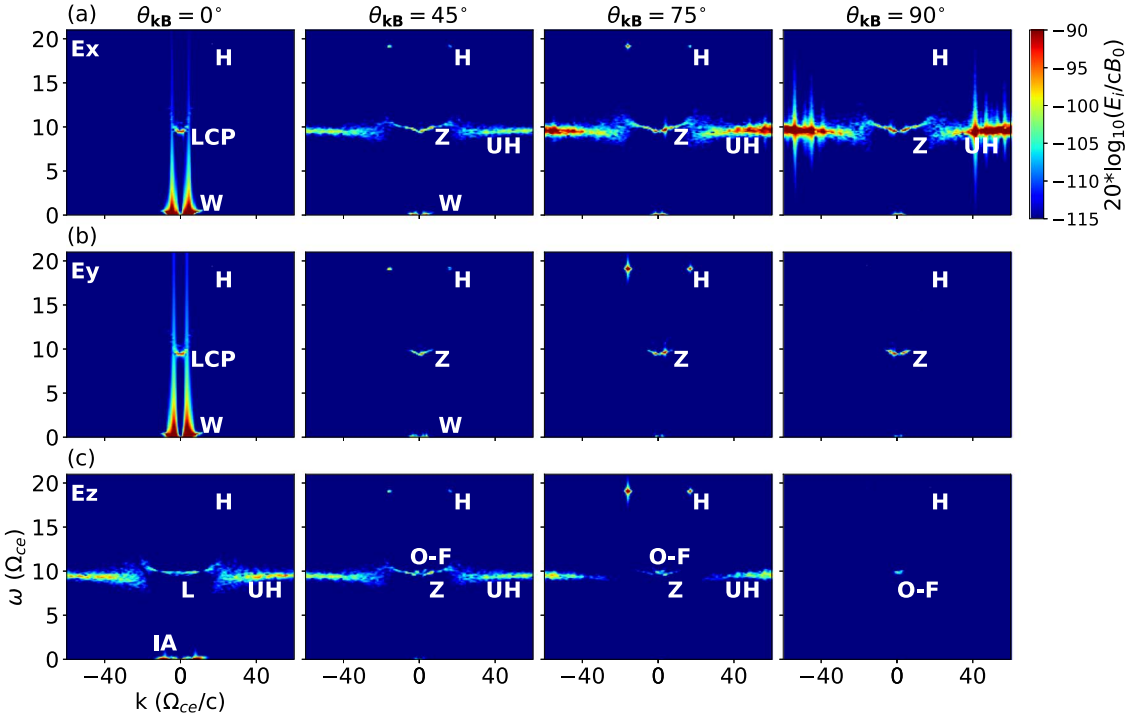

Figure 3. Wave dispersion diagrams of (a) E_x, (b) E_y, and (c) E_z over times $2500 < \omega_{pe}t < 3500$ along the directions specified in Figure 2(d). An animation of this figure is available. The video begins at $\theta_{kB} = 0^\circ$ and advances 5° at a time until ending at $\theta_{kB} = 180^\circ$. The realtime duration of the video is 15 s.

(An animation of this figure is available.)

resonance, as clearly seen from the dispersion analysis on the transverse component (E_y). The other part at large $|k|$ ($25\ \Omega_{ce}/c < |k| < 80\ \Omega_{ce}/c$) is the very strong UH mode around frequencies of [9, 10.2] Ω_{ce} (see, e.g., Andre 1985). In accordance with Figure 2, the UH waves result in the rise of E_x and E_z as already seen from Figure 1. At even larger $|k|$ ($>80\ \Omega_{ce}/c$), there exist some electron Bernstein modes which are in general weak in amplitude (not displayed here). Both the UH and electron Bernstein modes are electrostatic according to Fourier analysis.

At frequencies below 0.4 Ω_{ce}, the W mode arises at small wave numbers ($|k| < 10\ \Omega_{ce}/c$), mainly along the parallel direction. The W mode is dominated by strong magnetic oscillations, resulting in the rise of B_x and B_y in stage II as seen from Figure 1(e). This mode becomes the dominant one from stages II to III.

Above the dispersion curves of the L and Z modes, there exist signals of the X and O modes around ω_{pe}. In addition, along the dispersion curves of the X and O modes and at about twice of ω_{pe} (19.0 Ω_{ce}) a significant narrowband emission can be identified. This is the mode accounting for the H circle as viewed from panels (b)–(d) of Figure 2. The intensity of the F emission is about one order of magnitude and that of the H emission is about two orders of magnitude above the corresponding background noise level at the same position of $\omega - k$. This is revealed by comparing with those given by simulation of only background Maxwellian electrons. These F and H emissions are escaping waves and of major interest here. The F emission is considerably close to the Z and L modes in frequency, thus it is difficult to identify them clearly. Therefore we present a zoom-in view of the modes around ω_{pe} in Figure 4 and the accompanying movie.

In Figure 4, along the parallel direction, there exist the L mode carried by E_z and the left-circularly polarized (LCP) and right-circularly polarized (RCP) modes carried by E_x and E_y. The frequency of the L mode is about 9.8 Ω_{ce}, slightly below ω_{pe}. This is due to the relativistic effect of DGH electrons on plasma oscillation. In other words, the frequency at 9.8 Ω_{ce} is the plasma frequency of the present DGH system. This modification of plasma frequencies affects almost all wave modes presented here. For example, the cutoff frequency of LCP is now 9.3 Ω_{ce} and that of RCP is now 10.3 Ω_{ce}, as read from the figure. These values are lower than those given by the unmodified ω_{pe} by about 0.2 Ω_{ce}. In the following discussion, we use $\omega'_{pe} = 9.8\ \Omega_{ce}$ to represent the modified plasma frequency.

Along other propagating directions, the mode turns into the electromagnetic Z mode which contains significant oscillation in E_y. In addition, the Z mode also appears in E_x and E_y with comparable amplitude. Its intensity is strongest around the quasi-perpendicular ($\theta_{kB} = 75^\circ$) and perpendicular ($\theta_{kB} = 90^\circ$) directions, and weaker along quasi-parallel propagations according to the analysis with smaller θ_{kB} ($\leqslant 45^\circ$, not shown here). The frequency of the Z mode extends from $\sim$9.4 to $\sim$10.4 Ω_{ce}.

Both O and X modes can be easily identified from the dispersion curves shown in Figure 4. Their frequency ranges are [9.8, 10] Ω_{ce} and [10.3, 10.5] Ω_{ce}, respectively. It is obvious that the O mode mainly induces oscillations in E_z, while the X mode induces oscillations in both E_x and E_y with comparable amplitudes. The intensity of the O–F mode is about one order of magnitude above the background noise level, while the X–F mode is at almost the same level as the background. This can be seen from the temporal profiles of electric field energy of the various wave modes as plotted in Figure 1(f). As read from this figure, the saturation times (τ_S) of ECMI-excited wave modes, i.e., the UH, W, and Z modes, are about 1000, 2500, and 1800 ω_{pe}^{-1}, respectively. In addition, the e-folding growth time of

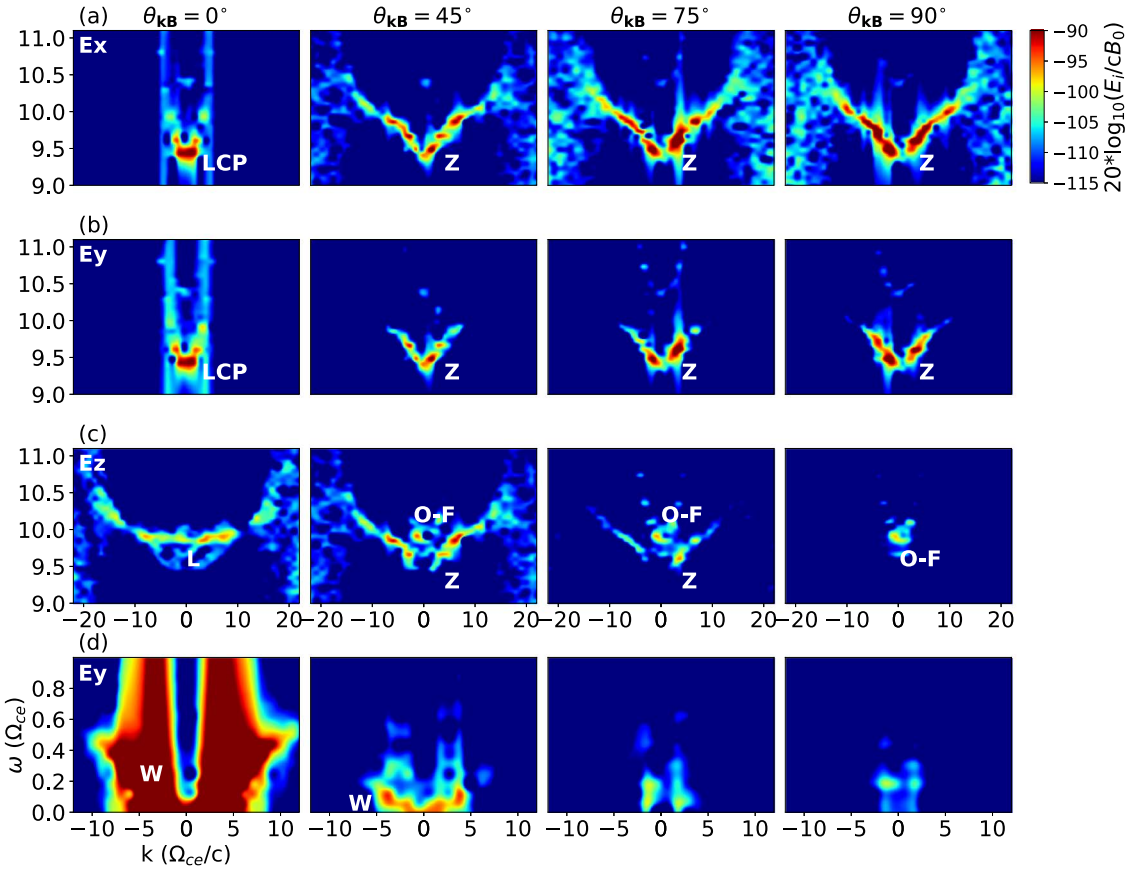

Figure 4. Wave dispersion diagrams of (a) E_x, (b) E_y, (c) E_z around the plasma frequency (ω_{pe}), and (d) E_y below the electron cyclotron frequency (Ω_{ce}) over times $2500 < \omega_{pe}t < 3500$ along the directions specified in Figure 2(d). An animation of this figure is available. The video begins at $\theta_{kB} = 0°$ and advances 5° at a time until ending at $\theta_{kB} = 180°$. The realtime duration of the video is 15 s.

(An animation of this figure is available.)

these modes can be obtained by fitting each energy curve with the exponential function e^{t/τ_G}, where τ_G represents the growth time during the linear stage of ECMI for the relevant wave modes (see, e.g., Aschwanden 1990). The fitting curves are plotted in Figure 1(f) as dotted lines, from which we get $\tau_G = 135\ \omega_{pe}^{-1}$ for the UH mode, 167 ω_{pe}^{-1} for the W mode, and 330 ω_{pe}^{-1} for the Z mode. Normalizing τ_S with corresponding τ_G, we have $\tau_S = 7.4$, 15, and 5.5 for the three modes respectively.

To separate the X and O modes from the H emission, we convert the E_x and E_y components into the left-handed (O) and right-handed (X) polarized components using the following equation:

$$E_{L,R} = \frac{1}{\sqrt{2}}(E_x \pm iE_y). \tag{3}$$

The result is shown in Figures 5(a) and (b). Both the X and O modes exhibit an obvious quadrupolar pattern with insignificant emission around the parallel and perpendicular direction. Their intensities are comparable.

4. Discussion on ECMI-induced Plasma Emission

Here we explain the obtained F–H plasma emission from the usual perspective of wave–wave coalescence. This process should satisfy the following resonance condition, in which subscripts "1" and "2" represent the two wave modes to coalesce and "3" represents the mode given by the coalescence:

$$\omega_1 + \omega_2 = \omega_3, \quad \boldsymbol{k}_1 + \boldsymbol{k}_2 = \boldsymbol{k}_3 \tag{4}$$

For the O–F emission ($|k| < 2\ \Omega_{ce}/c$, 9.8 $\Omega_{ce} < \omega < 10\ \Omega_{ce}$), the coalescence involves one mode around ω_{pe} and one mode below Ω_{ce}. Candidate modes around ω_{pe} are the L, Z, and UH modes, among which the intensity of the L mode is not stronger than the O–F emission and the UH mode is characterized by a very large k ($25\ \Omega_{ce}/c < |k| < 80\ \Omega_{ce}/c$). This indicates that the only mode around ω_{pe} that may satisfy the resonance condition is Z. On the other hand, the modes below Ω_{ce} are W and IA, both with $|k| < 15\ \Omega_{ce}/c$. Since the low-frequency IA mode is mainly along the parallel direction with $\omega < 0.1\ \Omega_{ce}$ and $4\ \Omega_{ce}/c < |k| < 5\ \Omega_{ce}/c$, for it to play a role, the Z mode along the parallel or quasi-parallel direction with frequency close to 9.8 Ω_{ce} and comparable wave number should be involved. Yet, according to the dispersion analysis, the Z mode satisfying the wave number resonance condition is basically the LCP part with a frequency less than 9.7 Ω_{ce}. Thus, the coalescence leading to O–F is most likely between Z and W. For the H emission ($16.0\ \Omega_{ce}/c < |k| < 16.7\ \Omega_{ce}/c$), both L and Z modes are weak in intensity for $|k| > 8\ \Omega_{ce}/c$, while UH features a large wave number. This indicates that the coalescence leading to H is most likely between almost counterpropagating UH modes. In Figures 5(c) and (d), we present schematics of possible configurations of wave vectors for modes of coalescence, overplotted onto diagrams of waves in relevant ranges of $k_{\parallel} - k_{\perp}$.

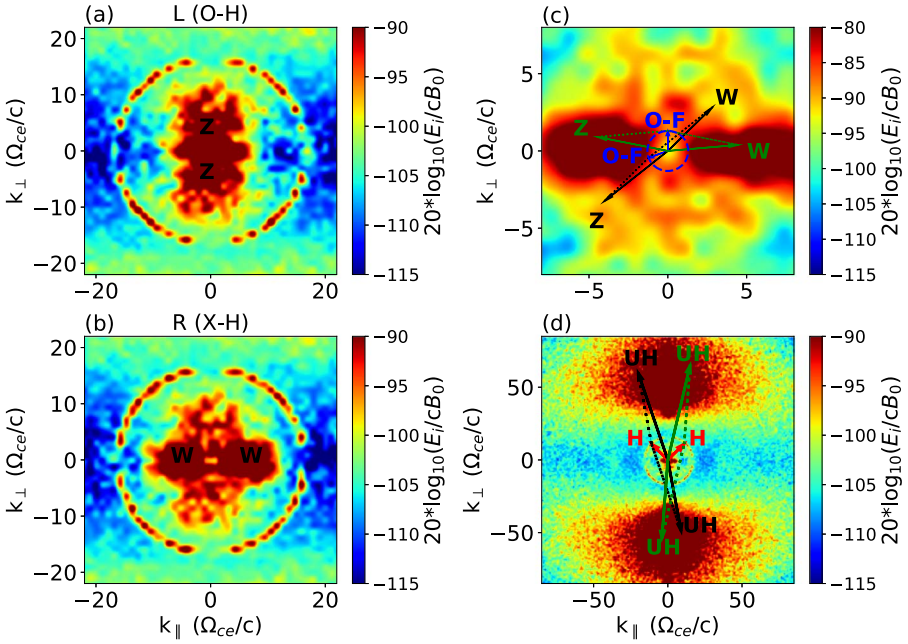

Figure 5. Maximum wave amplitude of the left-handed (a) and right-handed (b) polarized component in the ω domain as a function of $k_{\parallel}$ and $k_{\perp}$, obtained using Equation (3). Possible configurations of wave vectors of almost counterpropagating Z and W modes coalescing into the O–F mode (c), and of almost counterpropagating UH mode coalescing into the H mode (d).

Melrose (1975) pointed out that the only possible plasma emission process involving whistlers is the coalescence of a whistler with a Z mode, yet he deduced that such coalescence can occur only under implausibly restrictive conditions and therefore is unlikely to be significant, due to the specific small frequency range of whistlers meeting the resonance conditions. His conclusion was based on a simplified magneto-ionic dispersion relation for cold plasmas. Here the waves are resolved with 2D3V fully electromagnetic PIC simulations, thus thermal and kinetic effects have been adequately considered. In particular, the Z mode occupies a frequency range of 9.4–10.4 $\Omega_{\rm ce}$, which can exceed $\omega_{\rm pe}$ (or $\omega'_{\rm pe}$) and break the limits on frequency given by cold-plasma magneto-ionic theory. As seen, the Z-mode frequency obtained by PIC simulation partially overlaps with that of the O mode; this significantly relaxes the constraints on the frequency of the W mode, and invalidates the resonance condition (8a) given by Melrose (1975). Instead, the condition (8c) will apply to the situation investigated here. Further, the polarization of the Z mode is mainly in the sense of the O mode; this favors the wave scattering process from the Z to the O mode.

The energy transformation efficiency from energetic electrons to plasma waves via ECMI and from plasma waves to escaping electromagnetic radiation can be estimated from our simulation. Normalized by the initial kinetic energy of DGH electrons (E_{k0}), we obtain that $\sim$0.04% of E_{k0} has been converted to UH mode, $\sim$0.5% to W mode, and $\sim$0.00003% to Z mode, while the energy of the H emission is $\sim$0.03% of the energy of the UH mode, and the energy of the O–F emission is $\sim$2% of the energy of the Z mode and $\sim$0.0001% of the W mode. These values indicate that energy conversion efficiencies from energetic electrons to plasma radiation are quite low and the emission process investigated here only applies to radio bursts with relatively low intensity. This represents a general difficulty faced by most studies on plasma emission. For instance, in the latest PIC simulation of classical beam-driven plasma emission by Henri et al. (2019), it was found that the conversion efficiency from energetic electrons to the *H* band is $\sim 10^{-5}$ while the F emission is hardly discernible from their result.

DGH distribution is usually regarded as a two-sided loss-cone distribution which can develop within a magnetic trap. This trap exists pervasively in magnetized solar and stellar atmospheres, as well as in the magnetosphere of the Earth and other planets. In other words, the loss-cone type distribution of energetic electrons and the resultant radio emission may be common in space. However, the present result can only explain relatively weak emission. Future studies should explore approaches to enhance the emission intensity of both X and O modes. This can be achieved using other types of electron distribution, such as ring-beam or horseshoe distributions. These distributions have been used to explain solar microwave spikes, auroral kilometric radiation, and the Jupiter decametric burst, in plasmas of $\omega_{\rm pe}/\Omega_{ce} < 1$. Their effect on radiation in plasmas of $\omega_{\rm pe}/\Omega_{ce} > 1$ is yet to be explored.

5. Summary

The present study investigates radio emission in plasmas with a large $\omega_{\rm pe}/\Omega_{\rm ce}$, where classical ECME with direct amplification of radiation is not effective. We highlight possible underlying radiation mechanisms rather than applying the simulation to explain specific types of radio bursts. In this plasma regime, most earlier studies considered a beam of energetic electrons as the underlying driver of plasma emission. This is distinct from the radiation process investigated here, which is a two-step process energized by trapped electrons involving excitation of enhanced UH, Z, and W modes, and their coalescence. The excitation of these waves is due to cyclotron maser resonance (or instability), in the same physics as those releasing ECME. The coalescence of an almost counterpropagating UH mode is suggested to account for harmonic emission and the coalescence of the superluminal Z

mode and almost counterpropagating W mode for fundamental emission. This emission still belongs to the general type of plasma emission, yet is given by kinetic processes involving electron–cyclotron resonance, distinct from the classical paradigm. It can also be regarded as a combination of ECMI and nonlinear wave coupling. Future studies should explore the effect of various types of velocity distribution of energetic electrons, the effect of waves and turbulence, and inhomogeous distribution of background parameters such as density and magnetic field strength.

This study is supported by the National Natural Science Foundation of China (11790303 (11790300), 11750110424, and 11873036). X.K. also acknowledges the support from the Young Elite Scientists Sponsorship Program by the China Association for Science and Technology, and the Young Scholars Program of Shandong University, Weihai. The authors acknowledge the Tianhe-2 and Tianhe-3 systems for computational resources, the open-source VPIC code provided by LANL, and helpful discussions with Dr. Xiaocan Li (LANL), Prof. Quanming Lu (USTC), Prof. Kaijun Liu (SUSTech), Drs., Jianyuan Xiao (USTC), Xinliang Gao (USTC), Jicheng Sun (USTC), Yufei Hao (PMO), and Zongwei Yang (NSSC).

ORCID iDs

Yao Chen https://orcid.org/0000-0001-6449-8838
Xiangliang Kong https://orcid.org/0000-0003-1034-5857

References

Andre, M. 1985, JPlPh, 33, 1
Aschwanden, M. J. 1990, A&AS, 85, 1141
Benáček, J., & Karlický, M. 2018, A&A, 611, A60
Benáček, J., Karlický, M., & Yasnov, L. V. 2017, A&A, 598, A106
Bowers, K. J., Albright, B. J., Bergen, B., et al. 2008a, in SC '08: Proceedings of the 2008 ACM/IEEE conference on Supercomputing (New York: IEEE Press), 63, http://dl.acm.org/citation.cfm?id=1413435
Bowers, K. J., Albright, B. J., Yin, L., et al. 2008b, PhPl, 15, 055703
Bowers, K. J., Albright, B. J., Yin, L., et al. 2009, JPhCS, 180, 012055
Chen, Y., Du, G., Feng, L., et al. 2014, ApJ, 787, 59
Dory, R. A., Guest, G. E., & Harris, E. G. 1965, PhRvL, 14, 131
Dulk, G. A., & Marsh, K. A. 1982, ApJ, 259, 350
Feng, S. W., Chen, Y., Kong, X. L., et al. 2013, ApJ, 767, 29
Gaponov, A. V. 1959, IzRad, 2, 450
Ginzburg, V. L., & Zhelezniakov, V. V. 1958, SvA, 2, 653
Guo, F., Li, X., Li, H., et al. 2016, ApJL, 818, L9
Henri, P., Sgattoni, A., Briand, C., et al. 2019, JGRA, 124, 1475
Kong, X., Chen, Y., Feng, S., et al. 2016, ApJ, 830, 37
Kong, X., Chen, Y., Guo, F., et al. 2015, ApJ, 798, 81
Lee, J., Yoon, P. H., Seough, J., et al. 2018, JGRA, 123, 7320
Lee, K. H., Omura, Y., Lee, L. C., et al. 2009, PhRvL, 103, 105101
Lee, K. H., Omura, Y., & Lee, L. C. 2011, PhPl, 18, 092110
Li, C. Y., Chen, Y., Kong, X., et al. 2019, ApJ, 880, 31
Li, C. Y., Chen, Y., Wang, B., et al. 2017, SoPh, 292, 82
Li, X., Guo, F., Li, H., et al. 2015, ApJL, 811, L24
Liu, H., Chen, Y., Cho, K., et al. 2018, SoPh, 293, 58
Lv, M. S., Chen, Y., Li, C. Y., et al. 2017, SoPh, 292, 194
McLean, D. J., & Labrum, N. R. 1985, Solar Radiophysics: Studies of Emission from the Sun at Metre Wavelengths (Cambridge: Cambridge Univ. Press)
Melrose, D. B. 1975, AuJPh, 28, 101
Melrose, D. B. 1991, ApJ, 380, 256
Melrose, D. B. 2017, RvMPP, 1, 5
Melrose, D. B., & Dulk, G. A. 1982, ApJ, 259, 844
Pick, M., & Vilmer, N. 2008, A&ARv, 16, 1
Pritchett, P. L. 1986, JGR, 91, 13569
Ramaty, R. 1969, BAAS, 1, 290
Schneider, J. 1959, PhRvL, 2, 504
Sharma, R. R., & Vlahos, L. 1984, BAAS, 16, 536
Stepanov, A. V., Kliem, B., Krüger, A., et al. 1999, ApJ, 524, 961
Thurgood, J. O., & Tsiklauri, D. 2015, A&A, 584, A83
Treumann, R. A. 2006, A&ARv, 13, 229
Twiss, R. Q. 1958, AuJPh, 11, 564
Vasanth, V., Chen, Y., Feng, S., et al. 2016, ApJL, 830, L2
Vasanth, V., Chen, Y., Lv, M., et al. 2019, ApJ, 870, 30
Wagner, J. S., Lee, L. C., Wu, C. S., et al. 1984, RaSc, 19, 509
Wild, J. P., Smerd, S. F., & Weiss, A. A. 1963, ARA&A, 1, 291
Winglee, R. M. 1985, JGR, 90, 5141
Winglee, R. M., & Dulk, G. A. 1986a, ApJ, 310, 432
Winglee, R. M., & Dulk, G. A. 1986b, ApJ, 307, 808
Wu, C. S. 1985, SSRv, 41, 215
Wu, C. S., & Lee, L. C. 1979, ApJ, 230, 621
Yasnov, L. V., & Karlický, M. 2004, SoPh, 219, 289
Yi, S., Lee, S.-Y., Kim, H.-E., et al. 2013, JGRA, 118, 7584
Zlotnik, E. Y. 2013, SoPh, 284, 579